Available online at www.sciencedirect.com

ScienceDirect

IFAC Papers Online CONFERENCE PAPER ARCHIVE

IFAC PapersOnLine 50-1 (2017) 3971–3976

Robust Flare Control Design Using Structured $\mathcal{H}_\infty$ Synthesis: a Civilian Aircraft Landing Challenge

D. Navarro-Tapia * **P. Simplício** * **A. Iannelli** * **A. Marcos** *

* *University of Bristol, BS8 1TR, United Kingdom (Technology for AeroSpace Control (TASC), www.tasc-group.com; e-mail: diego.navarro-tapia/pedro.simplicio/andrea.iannelli/andres.marcos @bristol.ac.uk)*

Abstract: this paper addresses the flare design of a civilian aircraft within the benchmark proposed by ONERA and AIRBUS to enhance the robustness and capabilities of autoland control systems. The flare segment must perform soft landings within a desired range of touchdown points on the runway in the presence of parametric uncertainties, strong wind turbulence and ground effects. In this paper, a structured $\mathcal{H}_\infty$ approach based on the standard $\mathcal{H}_\infty$ formulation is explored for the vertical speed controller. In addition, some strategies to improve the robustness of the autoland control system against some critical parameters are described. Finally, the longitudinal performance and robustness of the control system are examined through nonlinear nominal simulations and Monte-Carlo analysis.

Keywords: aircraft landing challenge, flare control design, robust control

1. INTRODUCTION

The design of an autoland control system for a civilian aircraft is still a challenging task. The landing control system must be robust to a large range of operational parameter dispersion such as mass, center-of-gravity location, temperature, runway slope, runway altitude, wind disturbances, etc. This robustness must be proven through very demanding and tight requirements using a large number of Monte-Carlo simulations. Fortunately, the use of Instrument Landing Systems (ILS) has contributed to increase the operational domain of autoland control systems under critical weather and poor visibility conditions.

Nonetheless, the pilots still have to take control of the aircraft in severe crosswind conditions. Current civilian aircraft such as the A320 have a 20 kts crosswind limitation. In order to cope with this constraint, ONERA and AIRBUS proposed a benchmark to increase the robustness and the operational domain of autoland control systems with larger lateral wind ranges. Within this framework, this paper addresses the design of the longitudinal flare controller which is one of the most demanding segments of an autoland control system.

In the recent years, this problem has been overcome by using the so-called *variable tau flare law* (Lambregts, 1982). For example, under the project *Robust and Efficient Autoland control Laws design* (REAL), Looye and Joos (2006) used this flare design approach with good results. However, a complex controller optimization phase was necessary to fulfil all the longitudinal criteria. Other control techniques such as Linear Quadratic Regulator (LQR) have also been used in Sadat-Hoseini et al. (2013). One of the most extended robust control techniques is $\mathcal{H}_\infty$, which has also been successfully applied to flare design (Kaminer and Khargonekar, 1990). However, this theory generally provides high-order controllers with no structure. These constraints motivated the emergence of the so-called structured $\mathcal{H}_\infty$ approach (Gahinet and Apkarian, 2011), which allows to fix the order and structure of the controller. This new approach has been applied by Biannic and Apkarian (2001) to design a fixed-order vertical speed controller.

The structured $\mathcal{H}_\infty$ approach also incorporates new functionalities such as multi-channel and multi-model, which allows to optimize separate channels over different models. These new features were explored in Biannic and Roos (2015) with quite promising results for nominal performance without turbulence. However, direct application of this new formulation may overlook important cross-couplings between channels. This could be critical in multivariable control designs affected by many disturbances such as in the flare design.

This paper explores the flare control design using the structured $\mathcal{H}_\infty$ approach with a standard $\mathcal{H}_\infty$ formulation. In this case, the entire closed-loop is optimised, accounting for all the interactions between channels. It also aims to extend the work done in Biannic and Roos (2015) including strong turbulence and addressing robustness characteristics.

The layout of this paper is as follows. Firstly, the civilian aircraft landing challenge is introduced. Secondly, a flare design process based on the structured $\mathcal{H}_\infty$ approach but using the standard $\mathcal{H}_\infty$ formulation is presented. Finally, the flare design is analysed using nonlinear nominal simulations and validated through Monte-Carlo simulations.

10.1016/j.ifacol.2017.08.769

2. CIVILIAN AIRCRAFT LANDING CHALLENGE

The Civilian Aircraft Landing Challenge is a benchmark proposed by ONERA and AIRBUS to enhance the capabilities of auto-landing control systems. In this section, the aircraft model provided for the benchmark will be briefly described. Secondly, a description of the autoland segments will be presented and finally the validation method will be introduced.

2.1 The aircraft model

The aircraft model provided is a nonlinear six degree of freedom rigid-body aircraft. The model is based on the equations of motion, which account for gravity, engine thrust and aerodynamics. It also incorporates Dryden filters to represent wind turbulence and ILS noise, and environmental effects such as ground effect, temperature and airport characteristics (altitude, runway slope).

There are four actuators available: engine throttle position (δ_T), elevator (δ_E), ailerons (δ_A) and rudder (δ_R). The actuator dynamics are described as first-order systems limited in terms of rate and deflection.

The model inputs are the 4 actuators commands (δ_T, δ_E, δ_A, δ_R), the wind (W_x, W_y, W_z) and ILS noise (ω_{loc}, ω_{gld}). The model outputs are the load factors (N_x, N_y, N_z), the angular rates (p, q, r), the attitude angles (ϕ, θ, ψ), the angle-of-attack (α), the calibrated airspeed (V_c), the true airspeed (V_a), the ground speed (V_g), the vertical airspeed (V_z), the altitude (H), the landing gear height (H_{LG}), the route angle (χ) and the localizer and glide deviations (Δ_Y, Δ_Z).

A more detailed description of this model can be found in Biannic and Boada-Bauxell (2016).

2.2 Description of the landing phase

The autoland control system design is traditionally performed in the longitudinal and lateral axis separately considering a decoupling assumption. Both longitudinal and lateral controllers are generally structured using inner and outer control loops. The task of the outer loops is to provide inner loop commands to address the specific control objectives. On the other hand, the inner loops must track those commands providing robustness against disturbances such as turbulence and wind gusts.

The landing phase is divided into three phases:

A. Final approach phase: in this phase, the aircraft must track the glide-slope (vertical) and localiser (lateral) path commanded by the ILS while keeping the calibrated airspeed V_c constant and the sideslip angle β close to zero.

B. Flare phase: this phase replaces the longitudinal controller at 15 metres above the runway. In this short time interval, the flare segment controls the throttle position δ_T to set the engines to idle and the elevator deflection δ_E to reduce the vertical speed V_z.

C. Alignment phase: this phase replaces the lateral outer control loop at 9 metres above the runway to align the aircraft with the runway longitudinal axis.

2.3 Challenge validation

The assessment of this challenge is carried out through Monte-Carlo (MC) analysis using 2000 simulations. Each landing configuration is obtained by dispersing a set of 9 parameters (longitudinal and lateral wind levels, aircraft mass, center of gravity, runway altitude, temperature, runway slope, glide-slope angle and localiser displacement) according to a prescribed distribution. Besides, different wind and ILS noise seeds are used for each landing. A full description of the distribution for those parameters can be found in Biannic and Boada-Bauxell (2016).

For each landing, three longitudinal risk requirements are tested: height of the main landing gear over the runway 60 meters after the runway threshold (HTP60); landing point distance from the runway threshold (XTP); and vertical speed at touch-down (VZTP). These requirements evaluate the risk of short landings, long landings and hard landings, respectively. There are also three lateral risk requirements to satisfy. However, the focus of this paper will be on the longitudinal performance considering that both axes are decoupled. Discussions on the lateral performance will be presented in the Conclusion section.

This validation is performed in two phases:

(1) *Average Risk Level*: all the operational parameters are dispersed according to their distribution profile.
(2) *Limit Risk Level*: one of the parameters is set to its maximum/minimum value while the other parameters are dispersed according to their distribution.

For both average and limit risk phases, the probability level for each risk requirement reaching a limit value must be lower than the probabilities shown in Table 1.

Table 1. Risks evaluation

Evaluated risk	Probability	Average	Limit
Short landing	$P(HTP60 < 0m)$	10^{-6}	10^{-5}
Long landing	$P(XTP > 915m)$	10^{-6}	10^{-5}
Hard landing	$P(\lvert VZTP\rvert > 10ft/s)$	10^{-6}	-
	$P(\lvert VZTP\rvert > 12ft/s)$	-	10^{-5}

3. FLARE CONTROL DESIGN

This section describes the design procedure adopted for the flare segment. In less than 10 seconds, the vertical velocity must be reduced to avoid hard landings and structural damages. In addition, a safe touchdown point, around 400 m after the runway threshold, must be guaranteed to avoid short and long landings.

The flare controller must account for strong perturbations such as wind turbulence and ground effect. The latter consists in disturbances mainly dependent on altitude and angle of attack, which generate a pitching down moment and a lift increase. The flare manoeuvre is mainly directed by the elevator, since during flare the engines are set to idle position. All these conditions make flare control design a very challenging task.

The flare controller architecture is composed of three main blocks: vertical speed controller, vertical speed reference and throttle control (see Fig. 1). Each of these blocks are described next, concluding with the final joint tuning against some critical parameters performed to improve the robustness of the design.

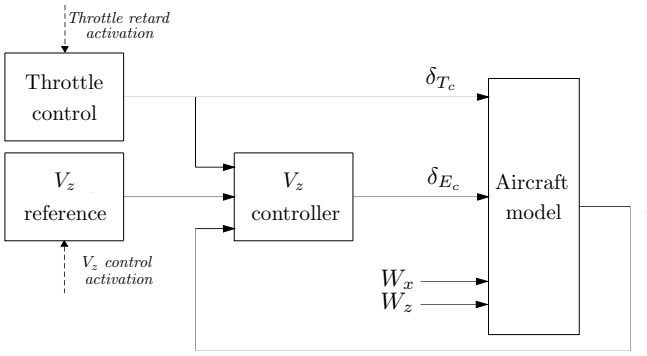

Fig. 1. Flare controller architecture

3.1 Vertical speed controller

This block controls the elevator deflection δ_E to reduce the vertical velocity and ensure an adequate touchdown point around 400 m.

The design model used in this work (see Fig. 2) is based on the one presented in Biannic and Roos (2015). In this paper, v_c and δ_{T_c} are considered as disturbance inputs. The former because it is highly perturbed by the ground effects and the latter to account for the engines deceleration dynamics. To do so, first, the nonlinear model is trimmed and linearised about a nominal flight condition. Then, this linearised model is simplified to consider only fast longitudinal dynamics and finally arranged to set v_c and δ_{T_c} as perturbations. Upper and lower case variables are used to distinguish between total and linearised values; subscripts c are used to denote commanded values. The resulting state-space model is given by:

$$\dot{x} = A \cdot x + B_u \cdot \delta_{E_c} + B_{dist} \cdot d \tag{1}$$

with $x = [v_z \ q \ \theta \ x_T \ x_E]^T$ and $d = [w_z \ v_c \ \delta_{T_c}]^T$.

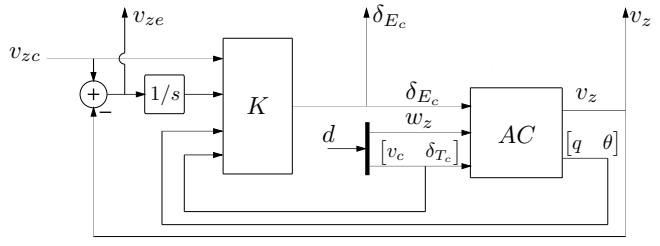

Fig. 2. Vertical speed controller design model

From Fig. 2, the controller K to be tuned has 6 inputs and 1 output, and its structure is as follows:

$$\delta_{E_c} = K \left[v_{zc} \ \int (v_{zc} - v_z) \ q \ \theta \ v_c \ \delta_{T_c} \right]^T \tag{2}$$

Unlike the multi-model and multi-channel structured $\mathcal{H}_\infty$ optimization shown in Biannic and Roos (2015), in this work a mixed-sensitivity structured $\mathcal{H}_\infty$ approach using a standard formulation is adopted. Using the multi-channel approach some important cross-couplings between channels may be overlooked (i.e. the channel between the perturbations and the actuator). Using the standard formulation, the full closed-loop system is considered, accounting for all the interactions between channels.

The control problem is formulated as shown in Fig 3, where the generalised plant model (P) is scaled through input and output weighting functions. The structured $\mathcal{H}_\infty$ optimisation consists of finding the controller $\hat{K}$ which minimises the $\mathcal{H}_\infty$ norm of the following cost function:

$$\hat{K} = min||\mathcal{F}_l(M, K)||_\infty \tag{3}$$

where M is the augmented closed-loop (including the weighting functions), K is the tunable structured controller and $\mathcal{F}_l$ denotes the lower Linear Fractional Transformation (LFT).

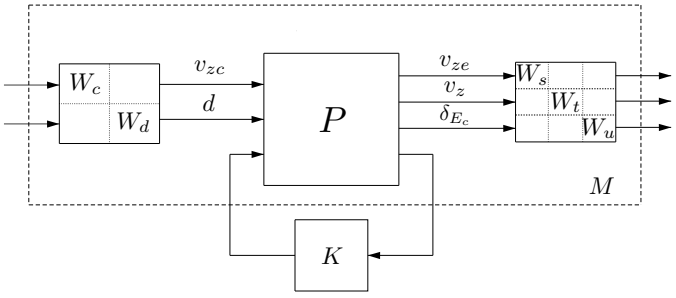

Fig. 3. Standard $\mathcal{H}_\infty$ interconnection

The structured $\mathcal{H}_\infty$ synthesis becomes an iterative process in which the weighting functions are shaped to obtain a good controller. Being a non-smooth approach, the initialisation of the optimiser is generally key for a successful design. In this work, the tunable controller K is initialised by zeros.

Although the choice of a static gain controller (0 states) is well appreciated by industry because every gain has a physical meaning and it allows a re-tuning phase after flight tests, better results were obtained using higher order controllers. In this paper, a second order controller is proposed. Next, the weighting functions used for this design are presented.

The input weighting functions are tuned to scale the closed-loop dynamics at the input side. In this design, the objective was to balance the input responses to facilitate the weight shaping for the elevator channel. The input weights are given by:

$$W_c = 0.3 \tag{4}$$

$$W_d = \begin{bmatrix} 1 & 0 & 0 \\ 0 & 0.15 & 0 \\ 0 & 0 & 0.5 \end{bmatrix} \tag{5}$$

Regarding the output weighting functions, W_s^{-1} and W_t^{-1} bound the classical sensitivity and complementary sensitivity functions of v_z, respectively. W_s^{-1} is a high-pass filter with low gain at low frequencies, -90 dB, to ensure a good tracking of v_z and 5 dB of high-frequency gain to achieve good robust stability. On the other hand, W_t^{-1} is a low-pass filter that forces roll off at high frequencies. In this design, W_s and W_t are given by:

$$W_s = \frac{s + 0.84}{0.56s + 8 \cdot 10^{-6}} \tag{6}$$

$$W_t = \frac{s + 0.88}{0.003s + 0.5} \tag{7}$$

On the selection of W_s and W_t a trade-off between nominal tracking performance and robustness emerged. Designs with a high and fast nominal tracking performance generally showed poor robustness in the MC simulations.

Hence, in order to improve the control system robustness, the tracking objective was relaxed.

Finally, the following high-pass filter is used for W_u to limit the elevator bandwidth and avoid saturation:

$$W_u(s) = \frac{\pi}{180}\frac{s+5}{0.001s+9} \tag{8}$$

3.2 Vertical speed reference

The v_z command is formed using an ideal second order model, whose initial value is the last value of v_z before the flare is activated and the final value is the target vertical speed of -0.75 m/s (-2.5 ft/s).

In order to avoid any overshoot in the tracking reference, the damping ratio is set to 1. In the selection of the natural frequency ω_{nv_z}, a design trade-off was found: faster commands (i.e. high ω_{nv_z}) imply softer but longer landings. A good balance between both requirements can be obtained using $\omega_{nv_z} = 2$ rad/s.

3.3 Throttle control

During flare segment, the engines activity is reduced to reach idle position. The throttles are open-loop retarded using an ideal second order model, which is traced from the last value of δ_{T_c} before the throttle control is activated to the necessary throttle position to reach $F_{eng} = 0$. This final value can be obtained using an approximation of the engine force expression found in (Biannic and Roos, 2015):

$$F_{eng}(kN) = 876 \cdot \delta_{T_c} - 852 \tag{9}$$

Since the engines dynamics are rather slow, it is sufficient to use a natural frequency of 1 rad/s. Similarly, the damping ratio is set to 1 to avoid backward engine forces.

3.4 Flare implementation

The flare controller described is then implemented on the benchmark nonlinear Simulink model, which is based on the overall architecture provided in Biannic and Boada-Bauxell (2016). The final approach inner-loop controllers (glide-slope and localiser) were also designed using the structured $\mathcal{H}_\infty$ optimisation framework, but also accounting for uncertainties to increase the robustness of the final approach segment. The reader is referred to Iannelli et al. (2017), where a robust analysis of the final approach controller can be found. The remaining control blocks, such as the final approach outer-loop and alignment controllers, are kept the same as in Biannic and Boada-Bauxell (2016).

3.5 Flare controller adjustment

Once the control design task has finished, a preliminary nonlinear analysis was carried out, showing a general good performance. Nonetheless, initial transients on the elevator responses were observed when the glide-slope and flare controllers are switched. In order to obtain a smoother transition, instead of using a binary switch, a simple second order interpolation between the outputs of both controllers was implemented.

In addition, a first MC analysis was performed (see Sec. 2.3 for details on the validation campaign). The developed flare controller fulfilled all the requirements except for three limit-risk cases, for each of which a bespoke tuning of the flare was performed as detailed next.

A. Minimum runway slope

Fixing the runway slope to its minimum value (-2%) resulted in soft but very long landings, violating the XTP requirement. This led to the conclusion that the runway slope was not being considered by the flare controller. In order to address this problem, the inertial vertical speed V_z was replaced by an estimate of the landing gear vertical speed V_{zLG}, which does take the runway slope into account. This estimate is computed as a pseudo-derivative of the height of the main landing gear (H_{LG}). A pure derivative was not implemented because it is not a proper transfer function. Noise has still to be managed by limiting the bandwidth of the pseudo-derivative. By applying this adjustment, this limit-risk case was successfully solved.

B. Maximum runway slope

Even after implementing V_{zLG}, the vertical speed performance was slightly violating the criteria for maximum runway slopes (2%). This was solved by increasing the flare activation height to 16.5 m. This modification gives the flare more time to reach lower vertical speeds and satisfy the $VZTP$ requirement.

C. Maximum longitudinal head wind

The maximum head wind (30 kts) is the most demanding limit-risk case for the longitudinal performance (see Section 4.2), showing a high dispersion in the runway touch-down point and violating the $VZTP$ requirement. This challenging case was tackled by reducing the throttle control activation height. This helps to further reduce the vertical speed at the expense of worsening XTP. A good balance between both requirements was found for a height of 13 m. Note that this modification implies that the throttle engines might not be set to idle before touchdown.

4. SIMULATION RESULTS AND DISCUSSION

In this section, the longitudinal performance and robustness of the full autoland control system are validated through nonlinear simulations and Monte-Carlo analysis.

4.1 Nonlinear simulation

Fig. 4 shows the nonlinear responses of the most relevant parameters for flare performance analysis. Three different nominal cases are considered: (i) without wind; (ii) with maximum tail wind, 30 kts, and lateral wind, 20 kts; and (iii) with maximum head wind, 10 kts, and lateral wind, 20 kts. For the sake of comparison, in all the plots the x-axis represents the distance to the runway threshold. Note that the flare segment is depicted in solid lines, whereas the final approach phase is shown in dashed lines.

The nominal simulation without turbulence (in black) shows an overall good performance. The aircraft performs a soft and smooth landing within the allocated runway range (see lower plot in Fig. 4). As it was stated in Sec. 3.1, a decision between good nominal tracking performance and global robustness was made in the design process. As a result, the tracking of V_{zLG} presents a steady-state error of 1.5 ft/s. Although it is a significant error, the $VZTP$ obtained is acceptable. Also note the good pitch response without overshoot rejecting the pitching down

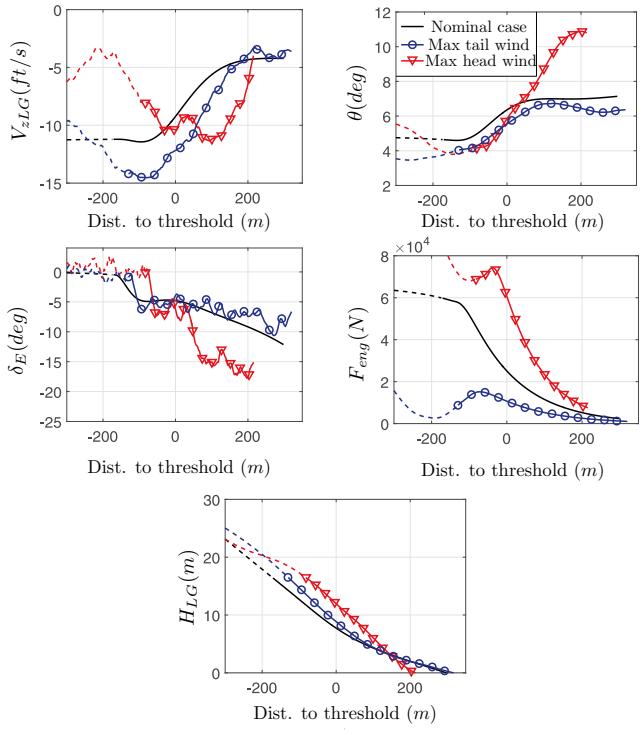

Fig. 4. Nonlinear simulations for nominal landing without and with maximum head and tail wind turbulence

moment originated by the ground effect (see the θ plot) and the good elevator response without any rate/deflection saturation (see δ_E in Fig. 4). Finally, it can be seen that the thrust engine force is decreased when the flare is activated (see the F_{eng} plot). However, the engines are not set to idle when the aircraft lands. This is a consequence of reducing the throttle retard activation height proposed in Sec. 3.5 to improve the limit risk robustness against maximum longitudinal head wind.

The flare control problem is still more challenging with the presence of strong winds. The controller should do the same job in less time because the aircraft is closer to the runway threshold (the flare activation is executed later because of the wind disturbances). However, the nominal simulations with turbulence shown in Fig. 4 also show acceptable performance despite the strong perturbations. Special attention to the smooth transitions achieved on the elevator responses between the glide and flare segments.

From Fig. 4, it can be concluded that the most demanding case is the simulation with maximum lateral and head winds (in red). This critical case requires more elevator deflection and more pitching moment, and it results in a harder and shorter landing than the other two cases. Nonetheless, the elevator actuation maintains the non-saturation response, the pitch moment does not decrease and V_{zLG} reaches a value lower than 10 ft/s (the limit value for the MC analysis).

4.2 Monte-Carlo assessment

A. Average risks level

In this MC assessment, the Gaussian distribution of the three longitudinal requirements described in Section 2.3 is evaluated over a set of 2000 landings.

For this test, 20 MC simulations of 2000 landings each were performed. Fig. 5 shows the 20 cumulative distribution plots superimposed. In order to satisfy the average requirements, the graphs should stay out of the yellow shaded area. It can be seen that all the average longitudinal requirements are fulfilled with very advantageous margins. Also notice the low dispersion between the different MC runs giving an insight of the design robustness.

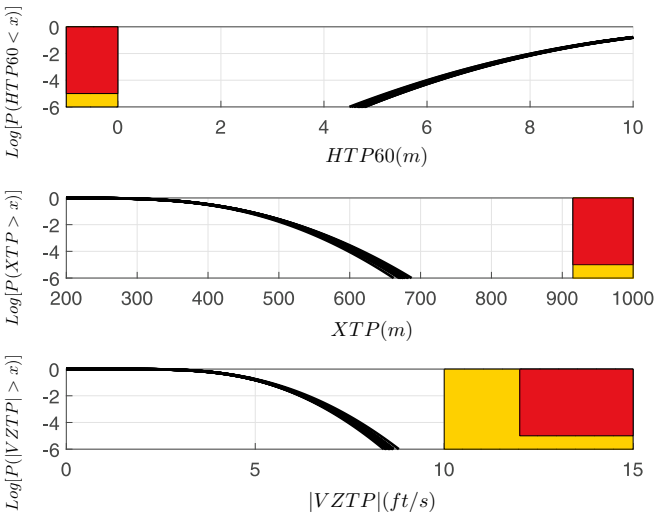

Fig. 5. Monte-Carlo analysis results (average risks)

Fig. 6 shows the Gaussian multivariable distribution of XTP and $VZTP$ (see upper plot) and its independent distributions (see lower plots). Note that for this figure only one of the 20 MC campaigns is considered. Observe the very good low dispersion for all the requirements.

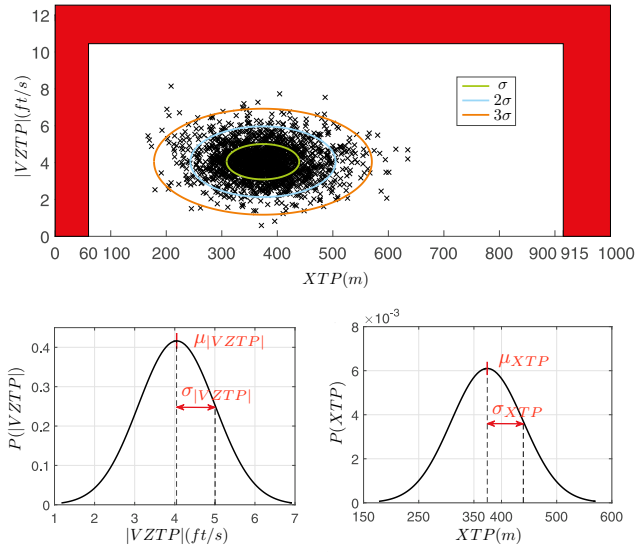

Fig. 6. Statistical analysis of longitudinal requirements using 2000 average risk landings

The mean values and standard deviations of XTP and $VZTP$ are listed in Table 2. It should be remarked that those values also satisfy the stochastic flare criteria used in the *REAL* project (Looye and Joos, 2006), corroborating the good average performance of the control system.

Table 2. Average-risk Gaussian distribution

Requirement	Mean	Standard deviation
XTP	375 m	65 m
$\|VZTP\|$	4.04 ft/s	0.95 ft/s

B. Limit risks level

For the limit risks, one of the operational parameters is fixed to its maximum and minimum value while the rest vary according to their statistical profile. Since there are 9 model parameters, this test consists of 18 MC campaigns (each of 2000 landings). Fig. 7 shows the distribution for each of the 18 limit risk analysis superimposed. In this case the limit requirements are delimited by the red shaded area. Again all the limit-risk requirements are fulfilled.

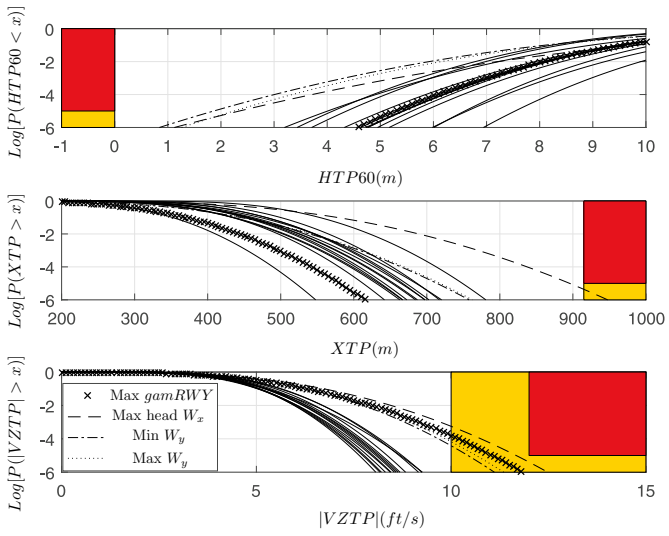

Fig. 7. Monte-Carlo analysis results (limit risks)

Fig. 7 also allows to extract worst-case operational parameters. For sake of clarity, only those parameters have been labelled in the figure. It can be concluded that the most critical parameter is the maximum head wind, being the worst limit-risk case for XTP and $VZTP$, and providing one of the worst performances in short landings (see upper plot). Other critical limit risks are the maximum and minimum lateral wind cases, both affecting $HTP60$. Finally, the maximum runway slope also affects the $VZTP$ as it was stated in Sec. 3.5.

Despite the graphs show a higher dispersion than the average case, the results are quite remarkable because all the limit-risk criteria are met and most of the limit-risk cases also satisfy the average-risk requirements (defined by the yellow shaded area), which are more demanding.

5. CONCLUSION

This paper presents the flare control design of an autoland control system within the framework of a civilian aircraft landing challenge proposed by ONERA and AIRBUS.

The use of the standard $\mathcal{H}_\infty$ formulation provides more insight for the weighting function selection to account for all the disturbance channels, in particular V_c which is highly disturbed by the ground effects. This helps to minimise the effects of perturbations and improve consequently the global robustness of the control system.

It should be remarked the difficult trade-off between nominal and robust design. The control law and implementation had to be modified to improve the system robustness versus three limit-risk cases which were not satisfied. In particular, the implementation of different activation heights for the vertical speed and the throttle control resulted in successful strategies to address those cases. In addition, the approach presented enables a smooth transition on the elevator channel between the glide and flare segments.

The longitudinal performance was evaluated through nonlinear simulations with and without turbulence. In all the cases, the responses show an overall good performance. Finally, the design robustness was validated through Monte-Carlo analysis. All the average- and limit-risk longitudinal requirements have been fulfilled. From both analyses, worst-case parameters could be extracted. The most critical limit-risk case is the maximum head wind, which presents a high dispersion in the touchdown point and satisfies $VZTP$ but only by a low margin.

Due to space constraints, the lateral performance is not evaluated in this paper. For the average risks level, all three lateral requirements are fulfilled with very advantageous margins. However, one of the lateral requirements (YTP - lateral deviation at touchdown) is violated in three limit-risk cases: maximum/minimum cross wind and maximum head wind. This is thought to be related to the very challenging lateral limit-risk requirements (confirmed by the benchmark developers to be likely exceedingly limiting). Future works will attempt to further improve the lateral controller.

REFERENCES

Biannic, J.M. and Apkarian, P. (2001). A new approach to fixed-order $\mathcal{H}_\infty$ synthesis: Application to autoland design. In *Proceedings of the AIAA control conference*.

Biannic, J.M. and Boada-Bauxell, J. (2016). A civilian aircraft landing challenge. On-line available from the aerospace benchmark section of the SMAC Toolbox, `http://w3.onera.fr/smac/`.

Biannic, J.M. and Roos, C. (2015). Flare control law design via multi-channel $\mathcal{H}_\infty$ synthesis: Illustration on a freely available nonlinear aircraft benchmark. In *Proceedings of the American Control Conference*.

Gahinet, P. and Apkarian, P. (2011). Structured $\mathcal{H}_\infty$ Synthesis in MATLAB. In *The* 18^{th} *IFAC World Congress*. Milan, Italy.

Iannelli, A., Simplício, P., Navarro-Tapia, D., and Marcos, A. (2017). LFT modelling and μ analysis of the aircraft landing benchmark. In *Proceedings of the* 20^{th} *IFAC World Congress*.

Kaminer, I. and Khargonekar, P. (1990). Design of the flare control law for longitudinal autopilot using $\mathcal{H}_\infty$ synthesis. In *Proceedings of the* 29^{th} *conference on decision and control*.

Lambregts, A. (1982). Avoiding the pitfalls in automatic landing control system design. In *AIAA Proceedings*.

Looye, G. and Joos, H. (2006). Design of autoland controller functions with multiobjective optimization. In *Journal of guidance, control and dynamics*, volume 29.

Sadat-Hoseini, H., Fazelzadeh, A., Rasti, A., and Marzocca, P. (2013). Final approach and flare control of a flexible aircraft in crosswind landings. *Journal of Guidance, Control, and Dynamics*, Vol. 36(4).